Marine Structures 87 (2023) 103332

Contents lists available at ScienceDirect

Marine Structures

journal homepage: www.elsevier.com/locate/marstruc

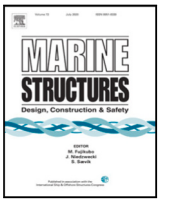

Hydrodynamic modelling of a multi-body wave energy converter using the Moving Frame Method

D.R. Lande-Sudall [a,*], J. Nyland [a], T.R. Rykkje [a], P.K. Stansby [b], T. Impelluso [a]

[a] Western Norway University of Applied Sciences, Department of Mechanical and Marine Engineering, Inndalsveien 28, 5063 Bergen, Norway
[b] University of Manchester, School of Mechanical, Aerospace and Civil Engineering, Oxford Road, Manchester, M13 9PL, UK

ARTICLE INFO

Keywords:
Wave energy
Multi-body dynamics
Moving Frame Method
M4

ABSTRACT

Significant wave energy conversion may be achieved with multiple floats with several modes of motion combining constructively to generate power. With the M4 system, power take off is at hinges to absorb resulting pitch motions. Complexity increases with number of floats and conventional vectorial multi-body dynamics may be conveniently replaced by the recently formulated moving frame method based on the calculus of variations to avoid free-body diagrams and joint reaction forces. Furthermore by utilising group theory to gather spatial rotations and angular velocities in a common structure, the obtained notation is general and straight-forward to apply for single and multi-body systems. This paper lays the foundations for incorporating hydrodynamic forces into the moving frame method. The method is applied to 3, 6 and 8 float cases in regular and irregular waves with results compared to the vectorial method and experimental measurements, showing close agreement. It is suggested that this is a more natural and general approach for complex multi-body, multi-hinge hydrodynamics systems.

1. Introduction

Compared with solar and wind energy, wave energy has the greatest power intensity [1]. In search of viable methods for energy harvesting, a multitude of wave energy converters have been investigated [2] and various group descriptions exist, based on principle of conversion, e.g. attenuators, point-absorbers, oscillating water columns and terminators [3]. Compared to near-shore sites, where around 70% of wave energy can be dissipated by bed-friction [4], the greatest wave energy resource is available offshore.

A particular problem for many wave energy converters (WECs) is the power capture limit imposed by their modes of motion [1]. For example a point absorber in heave has a capture width of $L/2\pi$ e.g. CorPower Ocean [5], in surge or pitch of L/π e.g. OSWEC [6], and in heave with surge and/or pitch L/π, for resonant conditions in regular waves of wavelength, L [1]. A two-body oscillating water column [7] is a form of heaving point absorber. Hinged beam devices, e.g. Pelamis and Mocean [8], have similar limits, $4L/3\pi$ for two uniform beams. In practical terms this restricts capacity to around 100 kW for many sites. Clearly this is an order of magnitude below wind turbine capacities which have increased from 5 to 15 MW recently, and larger capacities are planned. In order to match such capacities, WECs have been developed based on multiple floats and multiple modes of motion for which power from each component combines constructively. The M4 (multi-mode, moored, multi-body) is such a system, where power take-off (PTO) is located at hinges connecting beams between floats, driven by multiple modes. Up to eight floats with four PTOs have been considered to date [9].

Survivability for offshore WECs has also been problematic, as devices need to withstand high loads during storm conditions whilst being able to generate power on much lower mean conditions [8]. An important feature of M4 is good survivability performance.

* Corresponding author.
E-mail address: david.lande-sudall@hvl.no (D.R. Lande-Sudall).

https://doi.org/10.1016/j.marstruc.2022.103332
Received 15 October 2021; Received in revised form 5 September 2022; Accepted 28 September 2022
Available online 23 November 2022

Measurements indicate that extreme relative angle displacement between floats becomes saturated at about 40°, avoiding the need for end stops [10,11]. Analysis shows angular response to be predominantly linear [12], perhaps surprisingly, and direct linear modelling gives equivalent predictions, improved by a small physically realistic drag coefficient [13]. However mooring forces can be markedly nonlinear, with snap loads which, according to modelling [14], may be markedly reduced by elastic cables.

Clearly in moving from single floats, two-body oscillating water columns, or hinged raft types, to multiple bodies, complexity is increasing. The hydrodynamics for such multi-body systems presents a significant modelling challenge, whereby the response of each body is dependent on the diffraction and radiation effects of adjacent bodies. Additionally, simplified frequency-domain modelling cannot be relied upon for predicting accurate power capture due to significant nonlinear and transient interactions [15]. One approach to modelling is to follow a linearisation in time according to Cummins' equation [16] in order to translate from the frequency domain parameters, to parameters generalised over all wave frequencies in the time-domain.

Rigid body dynamics methods, used for analysing the relative motion and connections between such multi-body systems, also present another challenge. The equations of motion may be obtained through Newtonian mechanics or analytical mechanics. The former entails free-body diagrams of each component part, and their algebraic assembly into a series of equations and unknowns [17]. The latter, whether via Hamilton's Principle for conservative systems, or the Principle of Virtual Work for non-conservative systems, utilise the calculus of variations to provide the same equations, unencumbered by joint reaction forces. The equations are then typically solved in vectorial form, e.g. following the development in [18,19] and implemented in commercial programmes such as ProteusDS [20], SIMA [21] and FAST [22] as detailed in [23]. Whilst vectorial methods are reliable, the spatial rotations are not naturally handled, with a reliance on Quarternions or Plücker co-ordinates for example. These are intuitively difficult and cumbersome to extend as the number of interacting bodies and connections increases.

In this work, we employ the recently developed Moving Frame Method (MFM) [24] which is well suited to modelling multi-bodies and general connections. In order to extract the equations of motion, it is hypothesised that virtual rotations exist in a natural pair with a moment. Analogous to d'Alembert's Principle of Virtual Work, Jourdain [25] suggested the principle of virtual power, using the weighted form of Euler's equation with virtual angular velocity, whereby moment and angular velocity define the power instead of work. By recognising and implementing the structured group theory of Frankel [26], the Moving Frame Method (MFM) allows the equations of motion for multi-body spatial systems to be extracted in a generalised form, with notation remaining almost identical for 2D and 3D single bodies and multi-bodies [24]. This form of the equations of motion is ideal for rapid parallel processing, or for conversion into state-space form for control systems, and for use in structural finite element models. In this form, and by application to the M4 WEC, this paper builds upon the preliminary work of [27] to demonstrate how the MFM lends itself to modelling a large range of float configurations, without loss of generality. When utilising an identical numerical time integration scheme, the method also achieves faster run-times than an equivalent vectorial mechanics model.

In this paper, Section 2 introduces the mechanics of the M4 wave energy converter for three float configurations, as originally presented by [28,29]. The equations of motion for the vectorial mechanics model used by [29] are obtained following Newton mechanics and is summarised in Section 3, with a generalised form of the Moving Frame Method presented in Section 4. The time-domain hydrodynamics forces and numerical time-integration solver are presented in Section 5 before results for device response, forces and power-capture during regular and irregular sea-states are compared and experimentally validated in Section 6.

2. M4 wave energy converter

This paper considers three differing float configurations for the M4 WEC, named 111, 132 and 134. The terminology indicates the number of floats in each row, from bow to stern, as shown in Fig. 1. The floats are circular in cross section with rounded bases to minimise drag losses [30]. Float dimensions increase from bow to stern, which provides a range of natural periods in surge, heave and pitch, as well as serving to facilitate self-alignment with the predominant wave heading due to drift forces. This range of natural periods, along with mode coupling, results in a broadband response to allow power capture across a wide range of different spectral peak periods, T_P [29].

The longitudinal separation distance between the floats is around half a typical wavelength, such that forces and motions are predominantly in anti-phase with adjacent floats (see side profile in Fig. 2). The model-scale devices considered here are approx. 2.4 m long, representing a geometric scale factor of approximately 50. This is only an indicative scaling factor, since a full-scale device will be scaled to give optimal rated power capacity for the local resource and to minimise levelised-cost of energy.

Considering the 111 configuration, the stern float is connected via a rigid beam to a hinge above the mid float. For the 132 and 134 configurations, the longitudinal and vertical positions of the hinges remain the same as the 111 configuration. The transverse hinge positions are identified separately in Fig. 1. This arrangement of the stern floats allows relative rotation about each hinge and for activating the power take-off (PTO). For the full-scale device, the PTO would transform mechanical energy into electricity by extension and compression of a linear generator or a hydraulic-accumulator system [31]. For the model-scale device, this was implemented as a linear damper. During the experimental testing of [29], the device was also lightly moored with a single mooring line to the bow float to prevent longitudinal drift of the device position, to within about 1 cm. Mooring forces are driven principally by second-order difference frequency effects, and since this motion is small (approx. 1% of a wavelength), the mooring is neglected here.

The mass and moment of inertia for each float is given relative to each centre of mass in Table 1. For the vectorial model, the parallel axis theorem is used to reference these about the hinge, with values given in [29].

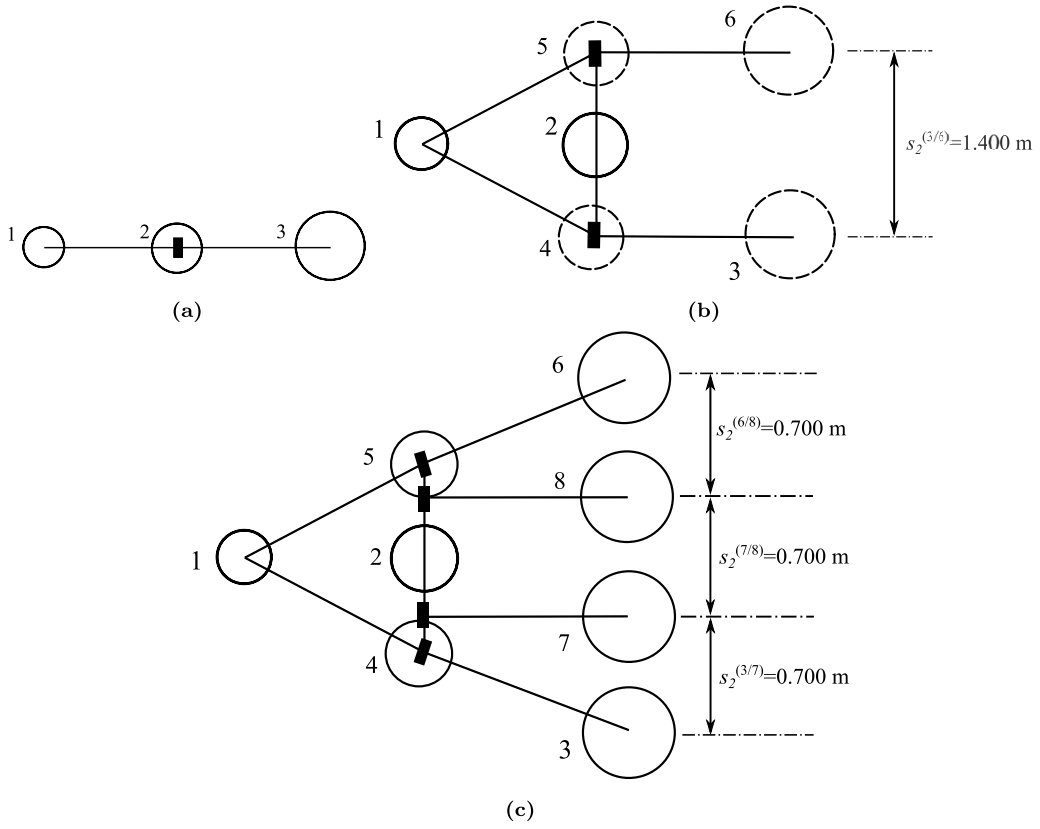

Fig. 1. Schematic diagram showing the three float configurations studied; (a) 111, (b) 132 and (c) 134. Float numbering is specified such that it is common to all layouts. the location of each PTO is marked with ▬. Longitudinal spacing between rows is the same for each configuration and as given in Fig. 2.

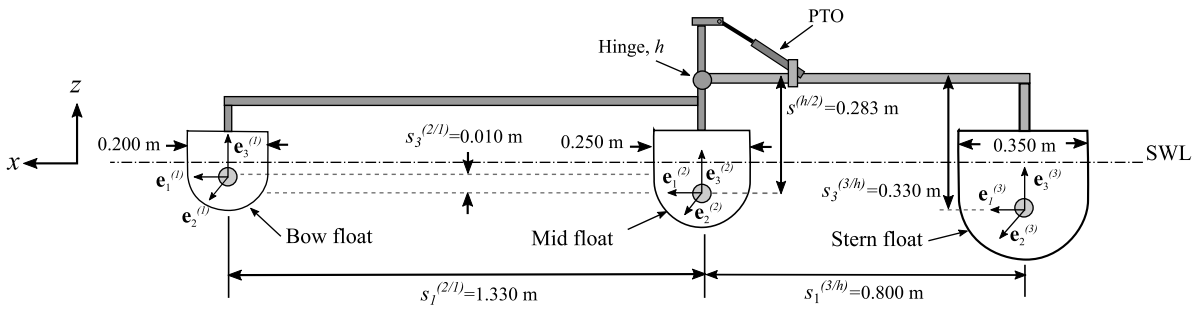

Fig. 2. Profile of the M4 wave energy converter, showing main parameter dimensions (model-scale) and the locations of moving frames placed at the centres of mass for each float ◯, along with the inertial Cartesian frame of reference.

Table 1
Float mass, moment of inertia and vertical centre of mass, z_M, relative to the still water line. Beam mass has been included by lumping half the mass of each beam onto each float mass.

Float no.	Diameter, m	Mass, kg	Moment of inertia, kg m^2	z_M, mm
1	0.20	2.345	0.204	−63.4
2,4,5	0.25	5.312	0.075	−73.3
3,6,7,8	0.35	17.520	0.614	−122.7

3. Vectorial mechanics model

The vectorial mechanics model used in this study has been developed in [29] and the reader is referred to this work for a complete description. In the following, only a brief description of the kinetics is provided to illustrate essential differences with the MFM which is introduced in Section 4.

The vectorial model starts by reducing the system of n individual floats into groups of rigidly connected bodies. For the 111-configuration, this results in two bodies, body-A and body-B, with n_A floats in body-A and n_B floats in body B. A moment balance Eq. (1) about the hinge is then considered for body-A, including all masses, $m_A = \sum_{i=1}^{n_A} m_i$, (e.g. ballast and beams):

$$-m_A \upsilon_A(\ddot{x}_O - \upsilon_A\ddot{\theta}) - m_A h_A(\ddot{z}_O - h_A\ddot{\theta}) + I_A\ddot{\theta}_A = M_{mech} + M_A - M_{hydro} \tag{1}$$

where υ_A and h_A are the vertical and horizontal distances of the floats from the hinge, O. The term in brackets, $(\ddot{x}_O - \upsilon_A\ddot{\theta})$, hence describes the linearised acceleration of the body about the hinge. M_{hydro} are the total horizontal, vertical and rotational moments due to all hydrodynamic sources (diffraction, added mass, radiation damping and buoyancy). Similar is done for body-B, with mass, $m_B = \sum_{i=1}^{n_B} m_i$:

$$-m_B \upsilon_B(\ddot{x}_O - \upsilon_B\ddot{\theta}) - m_A h_A(\ddot{z}_O - h_B\ddot{\theta}) + I_B\ddot{\theta}_B = -M_{mech} + M_B - M_{hydro} \tag{2}$$

These equations represent a sum of equations for each float in the body. The moments of inertia of each float from Table 1 are translated to the hinge position via the Parallel axis theorem. The equations are further complicated by the hydrodynamic coefficients in M_{hydro} being a function of θ_A, θ_B, $\ddot{x}_O$ and $\ddot{z}_O$, which are in-turn a vector summation of contributions from each float in the body and thus requires internal iterative corrector-loop to converge (see Fig. 3).

4. Introduction to the MFM

In this work, the equations of motion for the float system are obtained using the Moving Frame Method (MFM) in Dynamics. The MFM eschews a vector-based approach to dynamics, in favour of a matrix-based approach by leveraging three mathematical achievements of the last century:

- Cartan [32] suggested that all objects (even Euclidean space itself) be equipped with moving reference frames.
- Lie developed the Special Orthogonal and Special Euclidean Groups (SO(3) and SE(3) (along with their associated algebras: so(3) and se(3)). The MFM uses these algebras to connect the frames.
- A compact notation espoused by Frankel [26] enriches the MFM.

The MFM produces the same equations of motion as a traditional vector-based approach but in matrix form that is amenable to computation, with a consistent notational style that is the same for 2D dynamics, 3D dynamics, single body dynamics and multi-body dynamics. A summary of the method as deployed in the undergraduate curriculum is presented in [33], with a more advanced method for use in Multi-body dynamics in [24]. In the following, we move directly to the deployment of the MFM using the Special Euclidean Group applied to the M4 wave energy converter.

4.1. Generalised kinematics of M4

Fig. 2 illustrates the wave energy converter with moving frames, $\mathbf{e}^{(i)}$, positioned at the centre of mass of the ith float. The subscript indicates the direction of each of the orthogonal axes. The mass of each beam is accounted for by lumping half the mass to the two nearest floats, see Table 1 for the inertial properties.

Treating the floats as separate bodies is in contrast to the two-body system of the vectorial model. A similar grouping of rigidly connected bodies could be implemented in the MFM, however, this was found to be unduly onerous, especially when all the hydrodynamic coefficients are already provided relative to the individual float.

At time $t = 0$ s, an inertial frame is referenced from the first frame:

$$\mathbf{e}^I = \mathbf{e}^{(1)}(0) \tag{3}$$

The point-wise principle of Euclidean space allows this to serve as the inertial frame for the entire system.

For a moving frame attached to the centre of mass of body-i, an absolute frame connection matrix is defined, which contains the rotation and translation from the inertial frame:

$$E^{(i)}(t) = \begin{bmatrix} R^{(i)}(t) & x^{(i)}(t) \\ 0_3^T & 1 \end{bmatrix} \tag{4}$$

$R^{(i)}(t)$ is a rotation matrix, representing the rotation of the ith float, with $x^{(i)}(t)$ as the translation of the float.

The inertial and moving frame connections are related via the absolute frame connection matrix:

$$\begin{pmatrix} \mathbf{e}^{(i)}(t) & r^{(i)}(t) \end{pmatrix} = \begin{pmatrix} \mathbf{e}^I & \mathbf{0} \end{pmatrix} E^{(i)}(t) \tag{5}$$

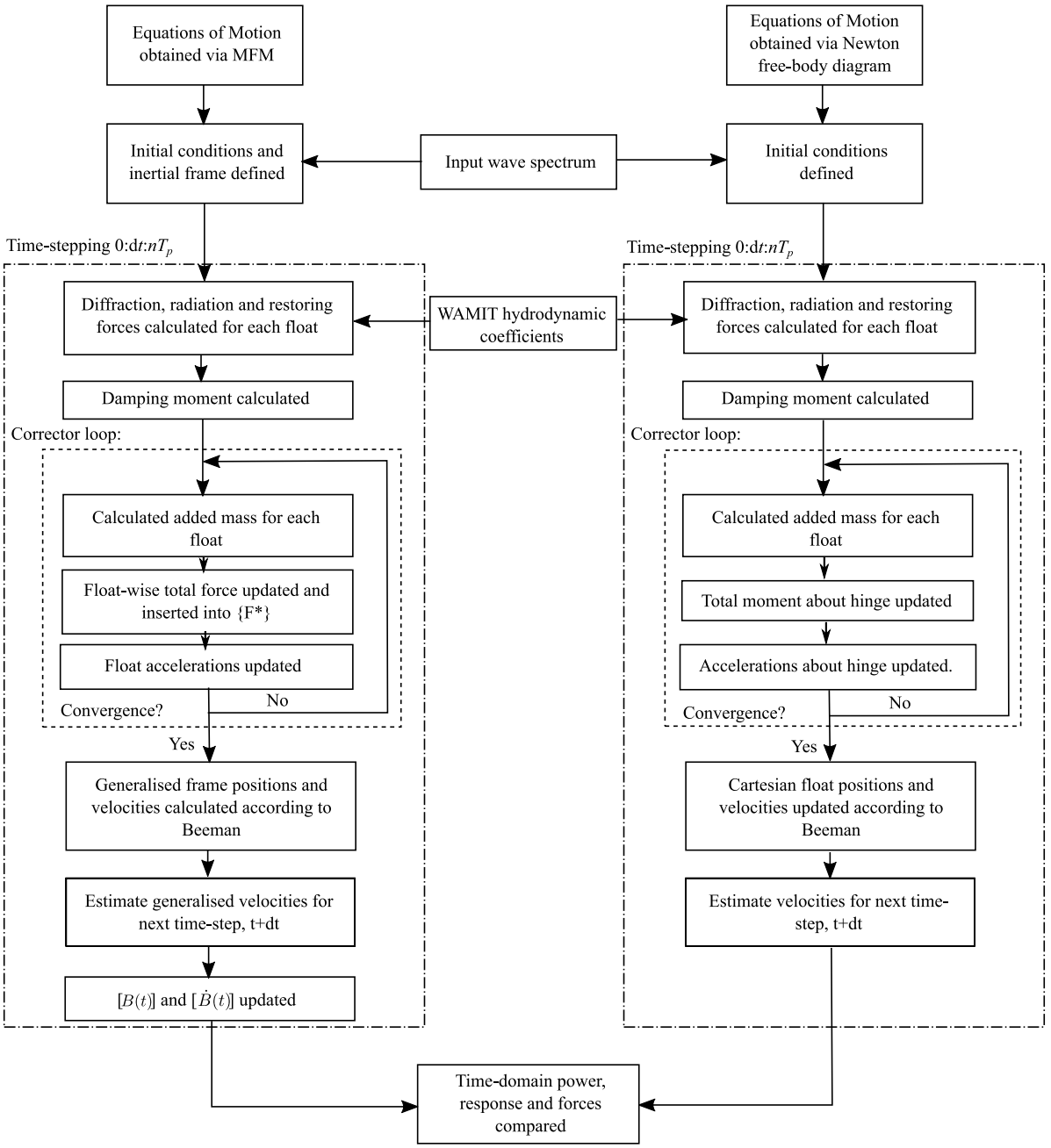

Fig. 3. Flow diagram for the two numerical codes, (left) using the MFM and (right) the vectorial method.

Similarly, the relative frame connection matrix, $E^{(j/i)}(t)$ relates the jth body frame connection to the ith body frame connection as shown:

$$\left(\mathbf{e}^{(j)}(t) \quad \mathbf{r}^{(j)}(t)\right) = \left(\mathbf{e}^{(i)}(t) \quad \mathbf{r}^{(i)}(t)\right) E^{(j/i)}(t) \tag{6}$$

To relate the jth frame to the inertial frame, the absolute frame connection matrix $E^{(j)}(t)$ is then found, in accordance with the closure property of the Special Euclidean group, SE(3), as:

$$E^{(j)}(t) = E^{(i)}(t)E^{(j/i)}(t) \tag{7}$$

A defining property of SE(3), is that the inverse matrix is known analytically. Since $E \in \mathrm{SE}(3)$, the inverse of the frame connection matrix can expressed as:

$$\left(E^{(i)}(t)\right)^{-1} = \begin{bmatrix} \left(R^{(i)}(t)\right)^T & -\left(R^{(i)}(t)\right)^T x^{(i)}(t) \\ 0_3^T & 1 \end{bmatrix} \tag{8}$$

Inserting Eq. (8) into (5) gives the inertial frame connection in terms of the moving frame connection:

$$\begin{pmatrix} \mathbf{e}^I & 0 \end{pmatrix} = \begin{pmatrix} \mathbf{e}^{(i)}(t) & \mathbf{r}^{(i)}(t) \end{pmatrix} \left(E^{(i)}(t)\right)^{-1} \tag{9}$$

This result is combined with the time rate of Eq. (5) to obtain the time rate of the frame connection, in terms of the frame connection itself:

$$\begin{pmatrix} \dot{\mathbf{e}}^{(i)}(t) & \dot{\mathbf{r}}^{(i)}(t) \end{pmatrix} = \begin{pmatrix} \mathbf{e}^{(i)}(t) & \mathbf{r}^{(i)}(t) \end{pmatrix} \left(E^{(i)}(t)\right)^{-1} \dot{E}^{(i)}(t) \tag{10}$$

The absolute time rate of frame connection matrix for the ith body, $\Omega^{(i)}$, is defined as the product of $(E^{(i)}(t))^{-1}$ and $\dot{E}^{(i)}(t)$. Thus, Eq. (10) can be rewritten as:

$$\begin{pmatrix} \dot{\mathbf{e}}^{(i)}(t) & \dot{\mathbf{r}}^{(i)}(t) \end{pmatrix} = \begin{pmatrix} \mathbf{e}^{(i)}(t) & \mathbf{r}^{(i)}(t) \end{pmatrix} \Omega^{(i)}(t) \tag{11}$$

$\Omega^{(i)}$ multiplied out in matrix form is:

$$\Omega^{(i)} = \begin{bmatrix} \overleftrightarrow{\omega^{(i)}(t)} & \left(R^{(i)}(t)\right)^T \dot{x}^{(i)}(t) \\ 0_3^T & 0 \end{bmatrix} \tag{12}$$

where the skew-symmetric angular velocity vector, $\overleftrightarrow{\omega^{(i)}(t)} = \left(R^{(i)}(t)\right)^T \dot{R}^{(i)}(t)$.

The component skew symmetric matrix is isomorphic to the angular velocity vector for the system; and for which the axis of rotation is time dependent. Eq. (11) then separates into the following two equations for each float:

$$\dot{\mathbf{e}}^{(i)}(t) = \mathbf{e}^{(i)}(t)\overleftrightarrow{\omega^{(i)}(t)} \tag{13}$$

$$\dot{\mathbf{r}}^{(i)}(t) = \mathbf{e}^{(i)}(t)\left(R^{(i)}(t)\right)^T \dot{x}^{(i)}(t) \tag{14}$$

During the experimental study of [29], small out-rigger buoys were mounted to the stern float to eliminate roll. Thus roll motion is ignored, as is the hydrodynamic contribution from these additional buoys. Only uni-directional waves are considered here, and so yaw and sway are neglected since these do not contribute to the power generation. This simplifies the linear velocity for the first float, and consequently for the second and third rows of floats. However, these rotations pose no issue for the MFM. Such a constraint of no roll is only to facilitate direct comparison of previous results from the traditional vector model with the MFM. After travelling the tree of the multi-link system, the algebra and group theory of SE(3) for the MFM provides the following equations (Eq. (15)–(27)) for the Cartesian angular and linear velocities for floats 1 to 8, respectively. They are expressed in terms of the minimal set of generalised velocities which the MFM readily accommodates. First, linear and angular velocity of float 1:

$$\dot{x}^{(1)}(t) = \begin{pmatrix} \dot{x}_1^{(1)}(t) \\ \dot{x}_2^{(1)}(t) \\ \dot{x}_3^{(1)}(t) \end{pmatrix}; \quad \omega^{(1)}(t) = \begin{pmatrix} \omega_1^{(1)}(t) \\ \omega_2^{(1)}(t) \\ \omega_3^{(1)}(t) \end{pmatrix} \tag{15}$$

Next, the linear and angular velocities of the second-row of floats:

$$\dot{x}^{(2)}(t) = R^{(1)}(t)\overleftrightarrow{s^{(2/1)T}}\omega^{(1)}(t) + \dot{x}^{(1)}(t) \tag{16}$$

$$\dot{x}^{(4)}(t) = R^{(1)}(t)\overleftrightarrow{s^{(4/1)T}}\omega^{(1)}(t) + \dot{x}^{(1)}(t) \tag{17}$$

$$\dot{x}^{(5)}(t) = R^{(1)}(t)\overleftrightarrow{s^{(5/1)T}}\omega^{(1)}(t) + \dot{x}^{(1)}(t) \tag{18}$$

$$\omega^{(2)}(t) = \omega^{(4)}(t) = \omega^{(5)}(t) = \omega^{(1)}(t) \tag{19}$$

Finally, the linear and angular velocities of the third-row of floats:

$$\dot{x}^{(3)}(t) = R^{(1)}(t)R^{(3/2)}(t)\overleftrightarrow{s^{(3/h)T}}\omega^{(3)}(t) + R^{(1)}(t)\overleftrightarrow{s^{(h/2)T}}\omega^{(1)}(t) + \dot{x}^{(2)}(t) \tag{20}$$

$$\omega^{(3)}(t) = \left(R^{(3/2)}\right)^T \omega^{(1)}(t) + \omega^{(3/2)}(t) \tag{21}$$

$$\dot{x}^{(6)}(t) = R^{(1)}(t)R^{(6/5)}(t)\overleftrightarrow{s^{(6/h)T}}\omega^{(6)}(t) + R^{(1)}(t)\overleftrightarrow{s^{(h/5)T}}\omega^{(1)}(t) + \dot{x}^{(5)}(t) \tag{22}$$

$$\omega^{(6)}(t) = \left(R^{(6/5)}\right)^T \omega^{(1)}(t) + \omega^{(6/5)}(t) \tag{23}$$

$$\dot{x}^{(7)}(t) = R^{(1)}(t)R^{(7/2)}(t)\overleftrightarrow{s^{(7/h)T}}\omega^{(7)}(t) + R^{(1)}(t)\overleftrightarrow{s^{(h/2)T}}\omega^{(1)}(t) + \dot{x}^{(2)}(t) \tag{24}$$

$$\omega^{(7)}(t) = \left(R^{(7/2)}\right)^T \omega^{(1)}(t) + \omega^{(7/2)}(t) \tag{25}$$

$$\dot{x}^{(8)}(t) = R^{(1)}(t)R^{(8/5)}(t)\overleftrightarrow{s^{(8/h)T}}\omega^{(8)}(t) + R^{(1)}(t)\overleftrightarrow{s^{(h/5)T}}\omega^{(1)}(t) + \dot{x}^{(5)}(t) \tag{26}$$

$$\omega^{(8)}(t) = \left(R^{(8/5)}\right)^T \omega^{(1)}(t) + \omega^{(8/5)}(t) \tag{27}$$

Note, the notation used above allows for individual motion of each float, however, due to the floats on row two being rigidly connected, floats 2 and 5 have identical kinematics. Similarly, floats on the third row have identical kinematics. The only difference between floats is the hydrodynamic forces experienced by each, which for uni-directional waves, there exists a symmetry plane about the transverse centreline. The notation adopted here enables future studies of individual float motions under omnidirectional waves, where symmetry planes do not exist.

In Cartesian coordinates, the velocity vector, $\{\dot{X}(t)\}$, contains three linear- and angular velocity components for each float and is therefore $6n\times1$ in size. The MFM adopts a minimal set of generalised velocities, $\{\dot{q}(t)\}$, to model the configuration of the system, consisting of surge, heave and pitch velocity of the bow float and pitch velocity of each stern float relative to the mid float, i.e. $(3+n)\times1$ in size. The Cartesian velocities are linearly related to the generalised velocities using the B-matrix:

$$\{\dot{X}(t)\} = \left[B(t)\right]\left\{\dot{q}(t)\right\} \tag{28}$$

The B-matrix for the 111-configuration, $[B]^{(111)}$ is found as:

$$\left[B\right]^{(111)} = \begin{bmatrix} e_1 & e_3 & \underset{3\times1}{0} & \underset{3\times1}{0} \\ \underset{3\times1}{0} & \underset{3\times1}{0} & e_2 & \underset{3\times1}{0} \\ e_1 & e_3 & R^{(1)}(t)\overrightarrow{s^{(2/1)}}^T e_2 & \underset{3\times1}{0} \\ \underset{3\times1}{0} & \underset{3\times1}{0} & e_2 & \underset{3\times1}{0} \\ e_1 & e_3 & B_{53} & B_{54} \\ \underset{3\times1}{0} & \underset{3\times1}{0} & \left(R^{(3/2)}(t)\right)^T e_2 & e_2 \end{bmatrix} \tag{29}$$

with

$$B_{53} = R^{(1)}(t)\left\{\left(\overrightarrow{s^{(h/2)}}^T + \overrightarrow{s^{(2/1)}}^T\right) + R^{(3/2)}(t)\overrightarrow{s^{(3/h)}}^T \left(R^{(3/2)}(t)\right)^T\right\}e_2 \tag{30}$$

$$B_{54} = R^{(1)}(t)R^{(3/2)}(t)\overrightarrow{s^{(3/h)}}^T e_2 \tag{31}$$

Where $\underset{3\times1}{0}$, e_1, e_2 and e_3 are defined as:

$$\underset{3\times1}{0} = \begin{pmatrix}0\\0\\0\end{pmatrix}, e_1 = \begin{pmatrix}1\\0\\0\end{pmatrix}, e_2 = \begin{pmatrix}0\\1\\0\end{pmatrix}, e_3 = \begin{pmatrix}0\\0\\1\end{pmatrix} \tag{32}$$

The B-matrix for the 132-configuration is found as:

$$\left[B^{(132)}\right] = \begin{bmatrix} & & [B]^{(111)} & & \underset{3\times1}{0} \\ & & & & \vdots \\ e_1 & e_3 & R^{(1)}(t)\overrightarrow{s^{(4/1)}}^T e_2 & \underset{3\times1}{0} & \underset{3\times1}{0} \\ \underset{3\times1}{0} & \underset{3\times1}{0} & e_2 & \underset{3\times1}{0} & \underset{3\times1}{0} \\ e_1 & e_3 & R^{(1)}(t)\overrightarrow{s^{(5/1)}}^T e_2 & \underset{3\times1}{0} & \underset{3\times1}{0} \\ \underset{3\times1}{0} & \underset{3\times1}{0} & e_2 & \underset{3\times1}{0} & \underset{3\times1}{0} \\ e_1 & e_3 & B_{11,3} & \underset{3\times1}{0} & B_{11,5} \\ \underset{3\times1}{0} & \underset{3\times1}{0} & \left(R^{(6/5)}(t)\right)^T e_2 & e_2 & \underset{3\times1}{0} \end{bmatrix} \tag{33}$$

with

$$B_{11,3} = R^{(1)}(t)\left\{\left(\overrightarrow{s^{(h/5)}}^T + \overrightarrow{s^{(5/1)}}^T\right) + R^{(6/5)}(t)\overrightarrow{s^{(6/h)}}^T \left(R^{(6/5)}(t)\right)^T\right\}e_2 \tag{34}$$

$$B_{11,5} = R^{(1)}(t)R^{(3/2)}(t)\overrightarrow{s^{(3/h)}}^T e_2 \tag{35}$$

The B-matrix for the 134-configuration, $[B]^{(134)}$ is found as:

$$\left[B^{(134)}\right] = \begin{bmatrix} & & [B]^{(132)} & & & \underset{3\times1}{0} & \underset{3\times1}{0} \\ & & & & & \vdots & \vdots \\ e_1 & e_3 & B_{13,3} & \underset{3\times1}{0} & \underset{3\times1}{0} & B_{13,6} & \underset{3\times1}{0} \\ \underset{3\times1}{0} & \underset{3\times1}{0} & \left(R^{(7/2)}\right)^T e_2 & \underset{3\times1}{0} & \underset{3\times1}{0} & e_2 & \underset{3\times1}{0} \\ e_1 & e_3 & B_{15,3} & \underset{3\times1}{0} & \underset{3\times1}{0} & \underset{3\times1}{0} & B_{15,7} \\ \underset{3\times1}{0} & \underset{3\times1}{0} & \left(R^{(8/5)}\right)^T e_2 & \underset{3\times1}{0} & \underset{3\times1}{0} & \underset{3\times1}{0} & e_2 \end{bmatrix} \tag{36}$$

with

$$B_{13,3} = R^{(1)}(t)\left\{\left(\overrightarrow{s^{(h/4)}}^T + \overrightarrow{s^{(4/1)}}^T\right) + R^{(7/2)}(t)\overrightarrow{s^{(7/h)}}^T\left(R^{(7/2)}(t)\right)^T\right\}e_2 \tag{37}$$

$$B_{15,3} = R^{(1)}(t)\left\{\left(\overrightarrow{s^{(h/4)}}^T + \overrightarrow{s^{(4/1)}}^T\right) + R^{(8/5)}(t)\overrightarrow{s^{(8/h)}}^T\left(R^{(8/5)}(t)\right)^T\right\}e_2 \tag{38}$$

$$B_{13,6} = R^{(1)}(t)R^{(7/2)}(t)\overrightarrow{s^{(7/h)}}^T e_2 \tag{39}$$

$$B_{15,7} = R^{(1)}(t)R^{(8/5)}(t)\overrightarrow{s^{(8/h)}}^T e_2 \tag{40}$$

The derivation of each B-matrix concludes the kinematics of the three configurations of floats considered. Each multi-body system can be described, uniquely, by a such a matrix. Furthermore, in cases where some variables may be prescribed, there exists a corresponding matrix to relate those variable to the Cartesian ones (but not in this case).

4.1.1. Equations of motion in MFM

The associated kinetics of M4 are now summarised, in order to arrive at the equations of motion in the MFM. After formulating the kinetic energy, δK, and replacing the potential energy with the work, δW (where the work accounts for the moment through the variation of the angular velocity), we start by asserting the Principle of Virtual Work, relating kinetic energy, δK and potential energy or work, δW:

$$\int_{t_0}^{t_1} \delta K(t)dt = -\int_{t_0}^{t_1} \delta W(t)dt \tag{41}$$

The kinetic energy is stated as:

$$\delta K(t) = \frac{1}{2}\left\{\delta\dot{X}(t)\right\}^T[M]\left\{\dot{X}\right\} \tag{42}$$

where the diagonal $6n\times6n$ mass matrix $[M]$ contains the individual masses, $m^{(i)}$, and moments of inertia, $J^{(i)}$, for each of the n-bodies in the system:

$$[M] = \begin{bmatrix} m^{(1)}I_3^{(1)} & \underset{3\times1}{0} & \dots & \dots & \underset{3\times1}{0} \\ \underset{3\times1}{0} & J^{(1)} & \underset{3\times1}{0} & \dots & \underset{3\times1}{0} \\ \vdots & \vdots & \vdots & \dots & \vdots \\ \underset{3\times1}{0} & \dots & \dots & m^{(N)}I_3^{(N)} & \underset{3\times1}{0} \\ \underset{3\times1}{0} & \underset{3\times1}{0} & \dots & \underset{3\times1}{0} & J^{(N)} \end{bmatrix} \tag{43}$$

For linear velocities, the variation of the time derivative is equal to the time derivative of the variation. However, to account for a restriction on angular velocities, proven by [34], the variation of the Cartesian velocities is written in terms of generalised coordinates as:

$$\{\delta\dot{X}\} = \frac{d}{dt}[B]\{\delta q(t)\} + [D][B]\{\delta q(t)\} \tag{44}$$

where the skew-symmetric $[D]$ matrix is introduced containing the angular velocity matrices for each frame.

A similar treatment for writing the Virtual Work in terms of generalised coordinates is pursued, with:

$$\delta W = \{q(t)\}^T\{F^*(t)\} \tag{45}$$

where the generalised force vector, $\{F^*(t)\}$ is related to the Cartesian force vector via the B-matrix, as $\{F^*(t)\} = [B]^T\{F(t)\}$. Inserting these expressions (42) and (45), into Eq. (41) and integrating by parts, the second order coupled differential equations of motion describing the kinetics of the system are then obtained:

$$\{\ddot{q}(t)\} = [M^*(t)]^{-1}\left(\{F^*(t)\} - [N^*(t)]\{\dot{q}\}\right) \tag{46}$$

with the following definitions:

$$[M^*(t)] \equiv [B(t)]^T[M(t)][B(t)]$$

$$[N^*(t)] \equiv [B(t)]^T\left([M][\dot{B}(t)] + [D(t)][M][B(t)]\right)$$

This results in one coupled, second order differential equation for each generalised coordinate. These equations are converted into a set of coupled first order differential equations by substitution. Further details of the complete derivation can be found in [27].

Comparing with traditional vectorial mechanics models (e.g. Eq. (1)), the analytical mechanics model of Eq. (46) contains an extra term, $[N^*(t)]\{\dot{q}\}$. This term arises from the intersection of variational methods, Eq. (41), with the MFM and the variation of the angular velocities. Unlike Newtonian methods, based on laws of force and moment vectors, the scalar properties of Lagrangian and Hamiltonian methods do not require free-body diagrams. Combined with the notation of SE(3) means the notation is generalised for 2D to 3D, single- and multi-body systems. Thus the method can be readily applied to a wide range of complex applications.

5. Time-domain hydrodynamic forces

For the hydrodynamic forces, a linearisation in time is used to convert the equations of motion from the frequency to time domain, following Cummins' equation [16] for Cartesian co-ordinates, Eq. (47). Here, the frequency-dependent added mass and radiation damping terms are decoupled into an added mass evaluated at infinite frequency, A_{ij}^{∞} and convolution integral representing the fluid 'memory effect' for past time, τ, evaluated to a lower limit of $\tau = t - 4T_p$.

$$\left(m + A_{ij}^{\infty}\right)\ddot{x}(t) + \int_{-\infty}^{t} L_{ij}(t-\tau)\dot{x}_j(\tau)d\tau + \rho g S x(t) = f_d(t) + f_{ext} \tag{47}$$

The impulse response function, L_{ij}, is pre-computed in discrete form as (48).

$$L_{ij}(t) = \frac{2}{\pi}\sum_{0}^{K} B_{ij}(\omega)\cos(\omega t)\Delta\omega \tag{48}$$

where $B_{ij}(\omega)$ is the frequency-dependent radiation damping coefficient for a single body of mass, m, oscillating in degree of freedom, i due to the interaction with degree of freedom, j, and obtained from the multi-body panel code, WAMIT for a set of $K = 200$ frequency intervals, evenly spaced between 0 and 4 Hz [29]. The third-term in Eq. (47) is the hydrostatic stiffness due to the change in buoyancy of a body with wetted surface area, S.

On the RHS of Eq. (47), the diffraction force, $f_d(t)$, for a random sea-state of K-linear components is found as the summation:

$$f_d(t) = \sum_{i=1}^{K} f_e(\omega_i)A_i\cos(\omega_i t + \phi(\omega_i) + \varphi_i) \tag{49}$$

where φ_i is a random phase angle between 0 and 2π radians. The frequency dependent excitation force coefficient, $f_e(\omega_i)$, and phase angle, $\phi(\omega_i)$, are computed in WAMIT. Coefficients obtained from WAMIT are defined about the centre of buoyancy, as opposed to the centre of mass which is required for the MFM. The WAMIT coefficients were obtained from earlier work [9,29] and this small translation has been neglected here, but it is noted that this could cause some minor discrepancies between the MFM and earlier results of [29].

The only external forces and moments, f_{ext}, considered are from the pitch moment due to the PTO. For the numerical comparisons in this paper, f_{ext} is computed by assuming a constant linear damping coefficient, $B_{PTO} = 6$ Nms/rad, multiplied with the relative angular velocity of the floats:

$$M_{PTO}(t) = -B_{PTO}\left(\omega^{(1)}(t) - \omega^{(3)}(t)\right) \tag{50}$$

During experiments, the value of the damping coefficient was found to vary [29], and so the reported values of B_{PTO} from [10,29] are used for comparing with the experimental results in Section 6.3.1. The power output is obtained from multiplication of the PTO moment and the relative angular velocity about the hinge, Eq. (51):

$$P_{tot} = M_{PTO}\left(\omega^{(1)}(t) - \omega^{(3)}(t)\right) \tag{51}$$

All other external forces and moments, such as drag and mooring line forces, are currently assumed negligible to aid direct comparison with [29]. Finally, Eq. (47) is directly inserted into the $F^*(t)$-term of the equations of motion for the MFM, (46), and in similarity with the vectorial method, requires an internal iteration to solve (see Fig. 3).

5.1. Numerical solver

Earlier work by [29] used Beeman's method to advanced the system of equations in time, which is a well-known method for molecular dynamics [35]. In contrast, [27] implemented a 4th-order Runge–Kutta method, RK4. In order to allow for direct code-comparison between the vectorial and MFM models, the same Beeman algorithm as used in [29] is implemented here, Eq. (52a).

$$q(t+\delta t) = q(t) + \delta t\left(\dot{q}(t) + \ddot{q}(t)\frac{\delta t}{2}\right); \tag{52a}$$

$$\dot{q}(t+\delta t) = \dot{q}(t) + \frac{\delta t}{2}\left(\ddot{q}(t) + \ddot{q}(t+\delta t)\right) \tag{52b}$$

This predictor–corrector algorithm which is exactly reversible, has a global truncation error of order $O(\Delta t^3)$ and was found to be more computationally stable for long time-series computations, as opposed to second-order methods, such as Midpoint, Heun's and Verlet integration, whose errors tended to exponentially grow after a long enough time-period.

An earlier implementation of the MFM used the symbolic toolbox in Matlab to maintain the absolute form of equations of motion [27]. However, this requires excessive computational resource and, as discovered when extending the configuration from three to six floats, the system becomes extremely time-consuming to solve. Instead, the complete computational code has been solved numerically here, using standard floating point, double precision for all terms.

Finally, a complete flow diagram of the two codes is shown in Fig. 3. This highlights the similarity in structure between the codes, despite solving contrasting equations of motion as observed by comparing Eqs. (1) and (46).

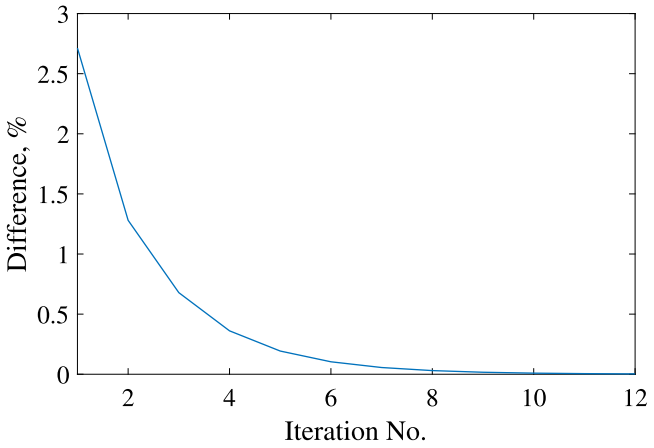

Fig. 4. Results showing percentage change in float 3's acceleration in pitch per iteration number, during one time-step of JONSWAP sea-state $H_S = 0.04$ m, $T_P = 1.0$ s, $\gamma = 1$.

Table 2
Regular and irregular waves modelled using the vectorial and MFM models.

	Wave height, m	Wave period, s	γ
Regular	$H = 0.04$	$0.4 \leq T \leq 2.06$	–
JONSWAP	$H_s = 0.04$	$0.8 \leq T_P \leq 1.8$	3.3
	$H_s = 0.04, 0.06, 0.08$	$0.8 \leq T_P \leq 1.8$	1.0

5.2. Numerical convergence

The vectorial model from [29] implemented a maximum of 10 iterations per time-step, as this was deemed to lead to adequate convergence to within plotting accuracy. In the MFM, a maximum deviation of 1% change in acceleration of the stern floats was implemented. On occasion, this led to the total number of iterations being greater than 10 iterations (conversely, sometimes less than 10). Fig. 4 shows an example of the percentage change in the acceleration about the y-axis of the stern float for one time-step during the $H_S = 0.04$ m and $T_P = 1.0$ s sea-state, where the total number of iterations was 12 (this was equivalent to the maximum number of iterations that occurred during this sea-state). It is clear that the percentage difference between 10 and 12 iterations is marginal. Given that this 1% convergence criterion was also defined for acceleration (not on float position), the sensitivity for float position would be even less. Both convergence criteria are therefore adequate. The computational speed of using either criterion was not investigated, since this was also apparently insignificant.

6. Results

6.1. Definition of test-cases

Table 2 shows the range of regular and irregular sea-states which have been run with both the vectorial and MFM models. For the irregular sea-states, theoretical JONSWAP spectra are defined with peakedness parameter $\gamma = 3.3$ for numerical comparisons in Section 6.3, and with measured spectra based on $\gamma = 1$ for experimental validation in Section 6.3.1.

6.2. Regular waves

To verify functionality of the MFM model, regular waves are first input, with wave periods equal to those at which WAMIT coefficients are available. Each regular wave is calculated over a total of $50T$ wave periods to allow the numerical simulation to settle. Fig. 5 shows an example regular wave case. The spin-up of the numerical simulation settles over the first 20 s. All time-averaged quantities are taken using the second half of the time-series. Floats 3 and 6 demonstrate practically identical pitch response, as expected due to these floats being symmetric to each another. The reason that these floats are not exactly equal appears to be due to minor differences in the WAMIT coefficients not being exactly symmetrical.

Time-averaged results of device response for the full range of regular wave simulations are compared against the response obtained for irregular waves in Section 6.3.2.

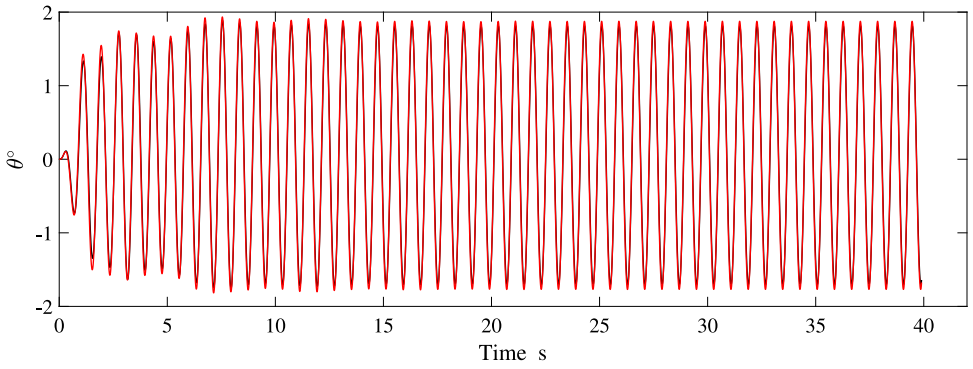

Fig. 5. Time-series pitch response of floats 3 and 6 of the 134 configuration for a regular wave with $T = 0.81$ s and $H = 0.04$ m (float 3 - black, float 6 - red).

6.3. Irregular waves

Having demonstrated symmetric and sinusoidal response in regular waves, the MFM model is compared against the vectorial mechanics model for irregular JONSWAP spectra of constant significant wave height, H_s and peakedness parameter, $\gamma = 3.3$ and varied peak period, T_P. In contrast to the regular wave tests, the irregular sea-states were defined as $100T_P$ long, to compare directly with [29].

Since the added mass force requires an internal corrector loop to iterate towards converged values of float accelerations, we present the time-variation of this force component only. Fig. 6(a) shows that the time-variation of added mass force in heave between the two codes is very similar, with a root-mean-square error, RMSE, between the two models less than 0.07 N. The observable discrepancies between the two models also appears greatest in the peaks, with the MFM generally proving more conservative than the vectorial model. However, the vectorial model used a fixed number of 10 iterations for the corrector loop, which was reported to be appropriate for convergence. However, the MFM is based on a convergence criterion requiring the change in float acceleration to be less than 1%, which frequently led to more than 10 iterations required for convergence. Needless to say, this discrepancy is small, and given that the vectorial model has been shown to slightly underestimate power production for this peak-period compared to experiment [29], the MFM model may be the more accurate implementation.

The insignificance of this discrepancy in added mass force between the MFM and vectorial models is further highlighted in the time-variation of heave response, which demonstrates excellent alignment (see Fig. 6(b)). Here, the RMSE is less than 3 mm, which is the same result reported in [27] for the symbolic code. This shows that no loss in computational accuracy has occurred by using a floating-point numerical implementation, compared to a symbolic implementation.

The time-varying quantities of power and relative angle about the hinge are averaged over the final $50T_P$ of the time-series for the full range of T_P defined in Table 2. The capture-width ratio, CWR, is defined in Eq. (53) and describes the ratio of average power absorbed to the power available in the sea-state, P_{wav}, normalised by a common device length, L_e, to allow cross-device comparison. $L_e = gT_e^2/(2\pi)$ is the deep water wave length corresponding to the energy period, T_e, where $T_e = 0.84T_P$ for JONSWAP spectra.

$$CWR = \frac{P_{av}}{P_{wav}L_e} \tag{53}$$

Fig. 7 demonstrates the well-reported broadband power capture of the M4, with increasing power output for increasing float numbers, and a corresponding increase in capture width ratio (exceeding 1 for the 134 configuration). In Fig. 8, the root mean square of the relative hinge angle, θ_{rms}, is presented since it is a valuable indicator for assessing the amount of absorbed power and mechanical loading of the hinge during device operation and survivability. It shows that θ_{rms} is around 2° for all configurations. Comparing between models from Figs. 7 and 8, very good agreement between the MFM and vectorial models is found for all time-averaged quantities of P_{av}, CWR and θ_{rms}. The greatest discrepancy occurs for θ_{rms} of the 111-configuration, between $T_P = 0.9$ and 1 s. This appears to be due to larger residual error in the MFM, related to the time-step for these sea-states being too large. Decreasing the time-step, δt, from $T_P/200$ s to $T_P/400$ s was found to bring the results in-line with the vectorial model. However, it is chosen to present only results for $\delta t = T_P/200$ s, to correspond with [29]. Small discrepancies on time-averaged quantities of the 132 and 134 configurations are also generally found for lower values of T_P. The source of this disparity is not clear. However, it is suspected it maybe due to the buoyancy centre being used as the reference for the hydrodynamic coefficients, instead of mass centre as required for the MFM. This will have a more significant impact for short wave periods where acceleration terms are generally greater. Indeed, it is known that the vectorial model under-predicts power at low T_P compared to experiment [29], so the MFM may be more representative here. Further comparisons to experimental measurements are studied in Section 6.3.1.

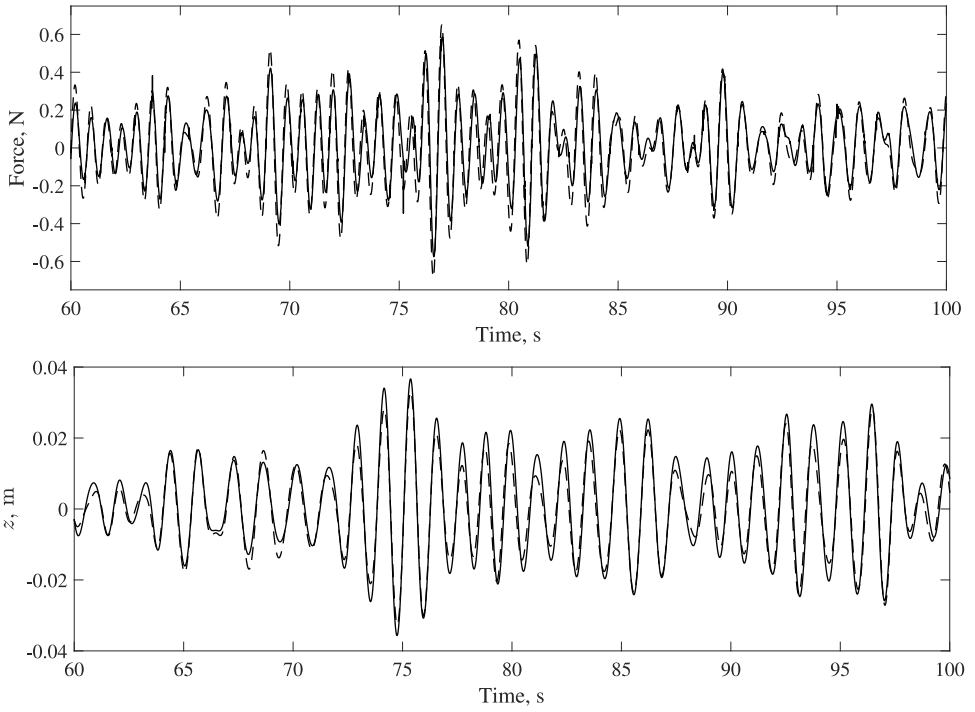

Fig. 6. Time variation of (a) added mass force, and (b) response for float 3 of the 111 configuration in heave, using the MFM (black solid line) and vectorial model (black dashed line) for $H_s = 0.04$ m and $T_P = 1.2$ s.

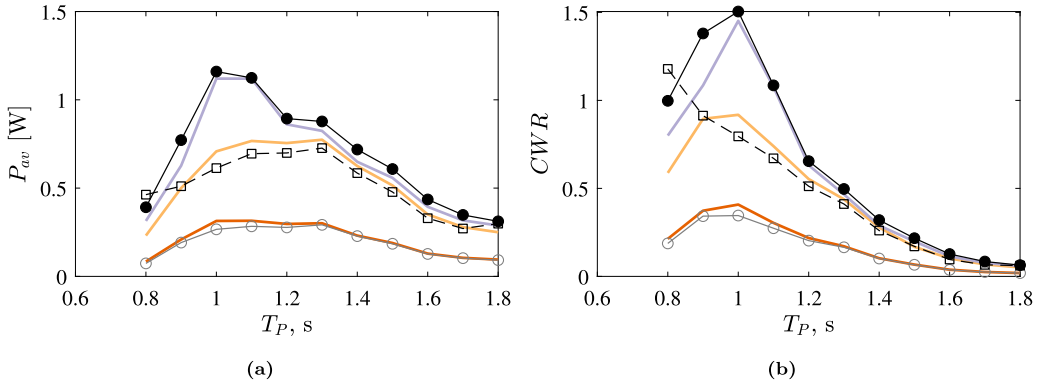

Fig. 7. Time-averaged power, P_{av} (a) and capture width ratio, CWR (b) obtained over last $50T_P$ seconds of the time series, for each of the three configurations: 134 (MFM ●—, vectorial —), 132 (MFM □– – –, vectorial —), 111 (MFM ◯—, vectorial —). P_{av} and CWR is obtained as the mean from all PTOs for the 132 and 134 configurations.

6.3.1. Experimental validation

To enable further validation of the MFM numerical model, experimental data for the 111 and 132 configurations operating in water depth, $d = 1$ m have been made available from [10,29]. Unlike the numerical comparisons for JONSWAP spectra with peakedness parameter, $\gamma = 3.3$, the comparisons in this section are for a wider broadband JONSWAP spectrum with peakedness parameter, $\gamma = 1$ (Pierson–Moskowitz), since these were available for both float configurations. The range of peak periods, $0.8 \geq T_P \geq 1.8$ s and significant wave heights, $0.04 \geq H_S \geq 0.08$ m, is the same for both configurations, however the time-series length is $100T_P$ for the 111-configuration and $120T_P$ for the 132-configuration. Time-averaged quantities are therefore calculated over the final half of the series, i.e. $50T_P$ and $60T_P$, respectively.

The data for the 111-configuration are from tests conducted at the University of Plymouth COAST ocean basin, and 132-configuration in the University College Cork LIR National ocean energy test basin. Whilst the measured spectra at both facilities were close to JONSWAP, the measured spectra have been used directly here for generating the input wave train. However, for presenting results on capture width-ratio, it is the theoretical wavelength, L_e based on energy period, $T_e = 0.78T_P$ (for $\gamma = 1$) which has been

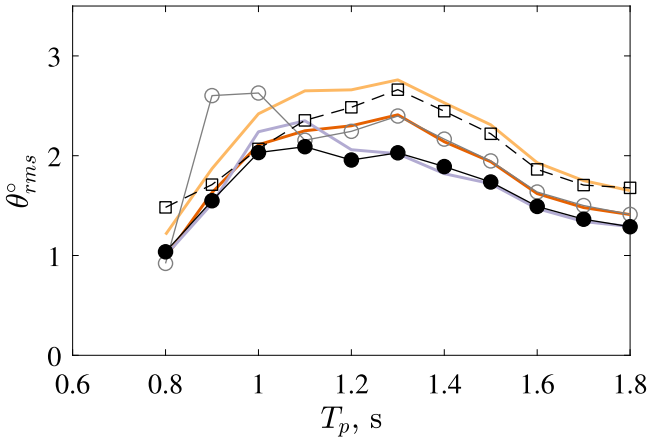

Fig. 8. Root-mean-square of the relative angle about the hinge, θ, obtained as average over last $50T_P$ seconds of the time series, for each of the three configurations (same line styles as Fig. 7).

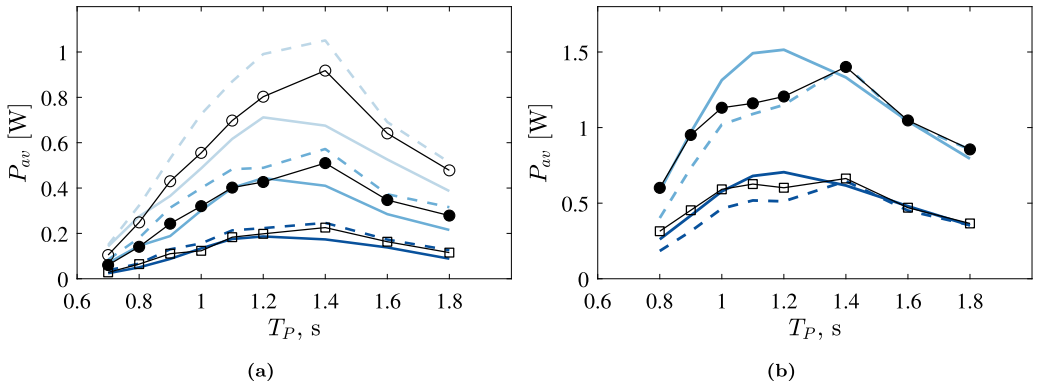

Fig. 9. Time-averaged power, P_{av} for (a) 111 and (b) 132 configurations, obtained over the last half of the time series with $\gamma = 1$ and H_S varying as 0.04 m (dark blue, MFM □——), 0.06 m (blue, MFM ●——) and 0.08 m (light blue, MFM ◯——). Experimental measurements are solid coloured lines and vectorial model dashed coloured lines.

used, to ensure a consistent definition across datasets. The measured time-averaged mechanical damping from each sea-state, as reported in [10,29] are used for the 111- and 132-configurations, respectively.

Fig. 9(a) for the 111-configuration, shows close agreement on time-averaged power between the vectorial and MFM numerical models, but there is a widening discrepancy with the experimental data as H_S increases. This discrepancy is most likely due to the limited validity of linear diffraction modelling as wave steepness increases. The presence of nonlinear waves become more significant for greater H_S, as well as nonlinear drag, wave run-up and greater nonlinear interaction between adjacent floats. Models considering higher-order wave kinematics and forcing are therefore important to develop. Additionally, the 111-configuration used in the Plymouth tests [29] had no outrigger buoys present, which would help to minimise roll. Roll may have acted to reduce actual power absorption and indeed, the no-roll numerical assumption would be invalid. Although, in a linear context, roll has no effect on power output and it has previously been discussed with use of the vectorial model [36], that the presence of roll does not result in a significant reduction in power absorption.

Due to the discrepancies found at high significant wave heights, only results for $H_S = 0.04$ and 0.06 m are compared for the 132 configuration (Fig. 9(b)). Here, both numerical models demonstrate similar trends in terms of under-prediction of power between $0.9 \geq T_P \geq 1.2$. This contrasts with the over-prediction seen for the 111-configuration. Since the 132 model is inherently stable, with larger gyration radius about the x-axis, this could indicate that the roll motion plays a more significant role in power absorption. However, the diffraction coefficients used for the 132 and 134 configurations were also adjusted to improve the hydrostatic stiffness arising from the centres of buoyancy and gravity not being coincident, which may give a marginal improvement in modelling accuracy [9].

The capture width ratio for $H_S = 0.04$ m is also compared for both the 111 and 132 configurations in Fig. 10, analogous to Fig. 7(b) where $\gamma = 3.3$. This highlights the excellent performance of the MFM model for small significant wave heights. Furthermore, all of the comparisons with experiment (Figs. 9–10) confirm the observed numerical behaviour, that the MFM seems to give more accurate predictions than the vectorial model at low T_P.

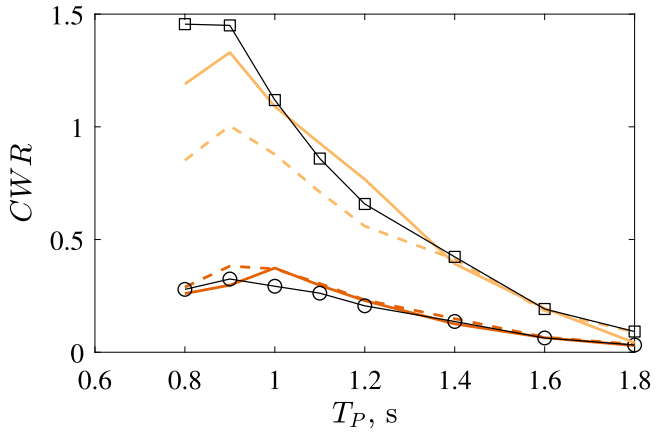

Fig. 10. Capture width ratio, CWR for 111 and 132 configurations, obtained over the last half of the time series for 111 (experiment —, MFM ◯—, vectorial - - -) and 132 (experiment —, MFM □—, vectorial - - -) configurations, obtained with $H_S = 0.04$ m.

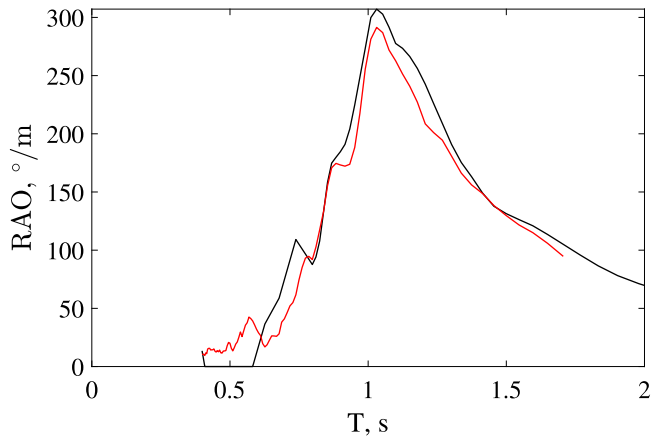

Fig. 11. RAO for the relative angle about the hinge, calculated between float 3 and 2 from the 134 configuration, obtained from regular waves (black) and an irregular JONSWAP spectrum with $T_p = 1.8$ s (red).

6.3.2. Spectral response

In this section, the response amplitude operator, RAO, of the relative angle about the hinge, θ, is presented. RAOs are useful for identifying the device response due to varying wave frequencies, and are defined as the square-root of the transfer function between the spectral response, $S_{\theta\theta}$ and spectral input of the undisturbed wave, S_{xx}:

$$RAO = \sqrt{\frac{S_{\theta\theta}}{S_{xx}}} \tag{54}$$

To minimise the effect of nonlinear interactions between the device response and input wave field on the generated RAO, the JONSWAP time-series with $T_P = 1.8$ s is chosen, since this is furthest away from the device's fundamental natural frequency.

An RAO can be equivalently found using a linear series of responses to regular waves, utilising the relation between spectral energy density and amplitude, A, of each angular frequency component, ω, Eq. (55).

$$S(\omega) = \sqrt{2A(\omega)d\omega} \tag{55}$$

Comparison between the two methods of RAO generation are compared in Fig. 11 for the 134 configuration, showing good agreement between the two. The discrepancies which occur are likely due to using relatively short time-series of irregular waves, such that the statistics are not fully stationary, as well as nonlinear frequency coupling effects not occurring for the regular wave method.

Similarly, the capture-width ratio can be obtained from irregular waves or regular waves, see Fig. 12. Due to the presence of a wider frequency band of wave components and available energy from these components in irregular waves, as well as nonlinear interactions, the 134 configuration is able to obtain higher capture-width ratio across all irregular wave periods compared to those from regular waves. This is for all wave periods except at $T = 1$ s, which corresponds to the device's eigenfrequency. Thus M4

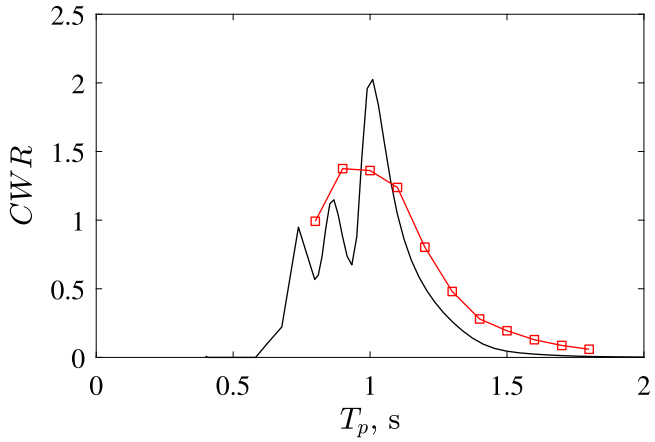

Fig. 12. Capture-width ratio calculated for the 134 configuration, obtained from regular waves (black) and irregular JONSWAP spectra (red), where the $T = T_p$ for regular waves.

Table 3
Computation times, in seconds, between the MFM and vectorial models for the 111-configuration. All computations were conducted on a simple laptop computer, with 16 GB RAM and an Intel i5 twin-core processor at 2.4 GHz clock-speed.

Model	Average computation time per simulated time-step, s
Vectorial	0.0052
MFM	0.0044

can obtain a greater CWR for regular wave conditions at this frequency, where energy is not spread across multiple frequency components. For periods greater than 1 s, the discrepancy in energy capture calculated using irregular waves versus regular waves of equivalent period, increases with increasing wave period, varying from 1.2 times greater at $T_P = 1.1$ s to over 8 times greater at $T_P = 1.8$ s. Similarly, the device power capture in irregular waves is smoother than for regular waves, across the full range of periods tested. As such, using a linear approach of regular wave testing would lead to a significant underestimate in energy yield for real seas, and possibly lead to poor control strategies being adopted for power-smoothing. These figures demonstrate the importance of considering both regular waves and full time-domain irregular sea-states for assessment of power capture from wave energy converters.

6.4. Computational expense

Both the vectorial and MFM model codes have been written for the 111-configuration in Matlab. All computations were conducted on a simple laptop computer, with 16 GB RAM and an Intel i5 twin-core processor at 2.4 GHz. The original vectorial model was written in Fortran77. Rather than restructuring the entire code to utilise Matlab's benefits of matrix-based computation, Fortran 'do' loops were simply preserved as 'for' loops in Matlab. For direct comparison of computational expense, a fixed total of 10 iterations of the corrector-loop was defined in both codes. The same approach for calculating the hydrodynamics terms and impulse response function was also used in both codes. However, as outlined above, the equations of motion of the MFM are inherently different to the vectorial model. This computational comparison therefore only offers a relative comparison between the two codes, as opposed to an absolute comparison of computational speeds, the latter of which could be significantly optimised for either code.

Table 3 shows that the MFM integrates in time approximately 15% faster than the vectorial model. For the complete JONSWAP time-series with $T_P = 1.2$ s, this led to a total run-time of approximately 60.4 s for the MFM and 87.6 s for the vectorial model, or 31% faster for the MFM overall.

Whilst this speed-up is desirable and possibly of benefit for large run-times, the code is already quick to run; between 4–8 min per sea-state for the 134 configuration solved with the MFM. So little computational benefit is gained here. Indeed, the main computational expense for all calculations is firstly in the generation of accurate hydrodynamic coefficients from diffraction modelling and in the computation of the impulse response function, which is not included in the times shown in Table 3, since these are the same for both dynamics solvers. The time to generate the impulse response function is of a similar order of magnitude to the total run-time per sea-state, e.g. 27.5 s for $T_P = 1.2$ s. Thus the computational benefits offered by the MFM appear limited, though it is emphasised that no optimisation of coding has been included. The MFM may offer greater nonlinear benefits on computational speed via parallel processing, than possible with the vectorial model. However, the main advantage of the MFM is the generality of the formulations of equations of motion, which remain the same for single and multi-bodies, in both two and three dimensions. Hence a robust, generic code can be generated faster, with possibility for automation of terms, and is thus arguably less prone to human-error. Furthermore, the regular structure of the SE(3) framework and avoidance of matrix inversion may be advantageous for use in state-space models to aid investigation of control strategies for the PTO.

7. Conclusion

The Moving frame method, MFM, in dynamics is a modern approach to rigid body dynamics and has been applied here to model the hydrodynamic interactions of a multi-body wave energy converter, M4. Using a Lagrangian frame of reference and regular matrix structure offered by the Special Euclidean group, SE(3), the method offers a generalised nomenclature, which is identical for single and multi-bodies, in two and three dimensional space. The resulting form of equations are directly equivalent to those obtained via traditional vectorial mechanics and thus do not require validation. This generality makes the MFM readily applicable to a host of complex mechanical interactions, that are often conceptually difficult to envisage.

This work has demonstrated a numerical implementation of the MFM, with hydrodynamic forces of added mass, radiation damping and hydrostatic stiffness applied for modelling the response of a multi-float wave energy converter in the time-domain. Three differing float combinations of the M4 WEC are modelled, demonstrating the extensibility of the method. Excellent agreement to existing vectorial modelling of the WEC is shown, with near-identical time-series in irregular JONSWAP sea-states and time-averaged power capture for a range of peak-periods. Against available model-scale experimental measurements, it appears that the MFM actually gives more accurate predictions than the vectorial model for low peak-periods. Additionally, the model was run for regular waves, to study the variation in device response and more specifically, capture-width ratio, compared to irregular wave tests. This demonstrated the importance of time-domain modelling in the consideration of power capture.

By leveraging a minimal set of coordinates and the power of analytically-known matrix operations, the MFM minimises the number of computations required to solve the system of equations. However, the computational advantage offered by the method, at least for short time-series durations, appears fairly limited given that the majority of computational time is dominated by the time required for obtaining the hydrodynamic coefficients. Nevertheless, the total time required to generate accurate and reliable codes using the MFM, should not be underestimated.

A simplification of no off-axis rotations was made, since these rotations were previously shown to be negligible. However, these will be implemented in future work, such as for studying floating offshore wind turbines with individual blade pitch control. Further work will focus on using the method to study mooring-line loads, with higher-order hydrodynamics force terms embedded. Coupling with a finite element method written using the MFM will also enable study of structural loads. Finally, the generality of the method lends itself for optimisation of further float arrangements and for studying more complex linkages and connectors, within the limits imposed by obtaining accurate hydrodynamic coefficients.

Declaration of competing interest

The authors declare that they have no known competing financial interests or personal relationships that could have appeared to influence the work reported in this paper.

Data availability

Data will be made available on request.

Acknowledgements

This research did not receive any specific grant from funding agencies in the public, commercial, or not-for-profit sectors. The authors declare no conflict of interest.

References

[1] Falnes J. A review of wave-energy extraction. Mar Struct 2007;20:185–201.
[2] Falcao A. Wave energy utilization : A review of the technologies. Renew Sustain Energy Rev 2010;14:899–918.
[3] López I, Andreu J, Ceballos S, Martínez De Alegría I, Kortabarria I. Review of wave energy technologies and the necessary power-equipment. Renew Sustain Energy Rev 2013;27:413–34.
[4] Greaves D. In: Greaves D, Iglesias G, editors. Wave and tidal energy. John Wiley & Sons, Inc.; 2018.
[5] Todalshaug JH, Asgeirsson GS, Hjalmarsson E, Maillet J, Moller P, Pires P, et al. Tank testing of an inherently phase controlled Wave Energy Converter. In: 11th European wave and tidal energy conference. Nantes; 2015.
[6] Yu YH, Hallett K, Li Y, Hotimsky C. Design and analysis for a floating oscillating surge wave energy converter. In: Proceedings of the international conference on offshore mechanics and arctic engineering - OMAE. 9B, (March). 2014.
[7] Gomes RPF, Henriques JCC, Gato LMC, Falcão AFO. Design of a Floating Oscillating Water Column for Wave Energy Conversion. In: EWTEC 2011 Proceedings. (September). 2011.
[8] Jin S, Greaves D. Wave energy in the UK: Status review and future perspectives. Renew Sustain Energy Rev 2021;143(September 2020):110932.
[9] Liao Z, Stansby P, Li G, Moreno EC. High-capacity wave energy conversion by multi-float, multi-PTO, control and prediction: Generalized state-space modelling with linear optimal control and arbitrary headings. IEEE Trans Sustain Energy 2021;12(4):2123–31.
[10] Carpintero Moreno E, Stansby P. The 6-float wave energy converter M4: Ocean basin tests giving capture width, response and energy yield for several sites. Renew Sustain Energy Rev 2019;104(January):307–18.
[11] Stansby P, Draycott S, Li G, Zhao C, Carpintero Moreno E, Pillai A, Johanning L. Experimental study of mooring forces on the multi-float wec m4 in large waves with buoy and elastic cables. Ocean Eng 2022;266:113049.
[12] Santo H, Taylor PH, Carpintero Moreno E, Stansby P, Eatock Taylor R, Sun L, et al. Extreme motion and response statistics for survival of the three-float wave energy converter M4 in intermediate water depth. J Fluid Mech 2017;813:175–204.

[13] Stansby PK, Moreno EC. Hydrodynamics of the multi-float wave energy converter M4 with slack moorings : Time domain linear diffraction-radiation modelling with mean force and experimental comparison. Appl Ocean Res 2020;97(January):102070.
[14] Stansby P, Moreno EC. Study of snap loads for idealized mooring configurations with a buoy, inextensible and elastic cable combinations for the multi-float m4 wave energy converter. Water (Switzerland) 2020;12(10).
[15] Folley M. Numerical modelling of wave energy converters: state-of-the-art techniques for single devices and arrays. 1st ed. Elsevier; 2016.
[16] Cummins W. The impulse response function and ship motions. Tech. rep., Schiffstechnik 9:; 1962, p. 101–9.
[17] Mei C. The applied dynamics of ocean surface waves. Singapore: World Scientific Publishing; 1989.
[18] Fossen TI. Nonlinear modelling and control of underwater vehicles (Ph.D. thesis), Norwegian Institute of Technology (NTH); 1991.
[19] Fossen TI. Handbook of marine craft hydrodynamics and motion control. 1st ed. John Wiley & Sons, Inc.; 2011.
[20] DSA. ProteusDS manual. Victoria, Canada; 2018.
[21] SINTEF Ocean. SIMO 4.16.2 theory manual. 2019.
[22] Jonkman JM, Buhl ML. FAST User's Guide - Updated August 2005. National Renewable Energy Laboratory.
[23] Bauchau O. Flexible multibody dynamics. Springer; 2011.
[24] Murakami H. A Moving Frame Method for Multi-Body Dynamics Using SE(3). Volume 4B: Dynamics, Vibration, and Control, ASME International Mechanical Engineering Congress and Exposition.
[25] Wittenburg J. Dynamics of multibody systems. 2nd ed. Springer; 2008.
[26] Frankel T. The geometry of physics, an introduction. Cambridge University Press; 2011.
[27] Nyland J. Implementation of hydrodynamic forces into the Moving Frame Method for analysis of multi-body wave energy converters (Ph.D. thesis), (June). University of Bergen; 2020.
[28] Stansby P, Moreno EC, Stallard T. Capture width of the three-float multi-mode multi-resonance broadband wave energy line absorber M4 from laboratory studies with irregular waves of different spectral shape and directional spread. J Ocean Eng Mar Energy 2015;1(3):287–98.
[29] Stansby P, Moreno EC, Stallard T. Large capacity multi-float configurations for the wave energy converter M4 using a time-domain linear diffraction model. Appl Ocean Res 2017;68:53–64.
[30] Gu H, Stansby P, Stallard T, Carpintero Moreno E. Drag, added mass and radiation damping of oscillating vertical cylindrical bodies in heave and surge in still water. J Fluids Struct 2018;82(1):343–56.
[31] Gaspar JF, Stansby PK, Calvário M, Guedes Soares C. Hydraulic Power Take-Off concept for the M4 Wave Energy Converter. Appl Ocean Res 2021;106(December 2019).
[32] Cartan E, Magnon A, Ashtekar A, Trautman A. On manifolds with an affine connection and the theory of general relativity. Napoli: Bibliopolis; 1986.
[33] Impelluso TJ. The moving frame method in dynamics : Reforming a curriculum and assessment. Int J Mech Eng Educ 2018;46(2):158–91.
[34] Holm DD. Geometric mechanics - part II: Rotating, translating and rolling. 2nd ed. 2011, p. 1–390.
[35] Beeman D. Some Multistep Methods for Use in Molecular Dynamics Calculations. J Comput Phys 1976;20:130–9.
[36] Sun L, Zang J, Stansby P, Moreno EC, Taylor PH, Taylor RE. Linear diffraction analysis of the three-float multi-mode wave energy converter M4 for power capture and structural analysis in irregular waves with experimental validation. J Ocean Eng Mar Energy 2017;3(1):51–68.